DE GRUYTER Nanophotonics 2021; 10(1): 697–704

Research article

Qinghua Song, Samira Khadir, Stéphane Vézian, Benjamin Damilano, Philippe de Mierry, Sébastien Chenot, Virginie Brandli, Romain Laberdesque, Benoit Wattellier and Patrice Genevet*

Printing polarization and phase at the optical diffraction limit: near- and far-field optical encryption

https://doi.org/10.1515/nanoph-2020-0352
Received June 29, 2020; accepted July 8, 2020

Abstract: Securing optical information to avoid counterfeiting and manipulation by unauthorized persons and agencies requires innovation and enhancement of security beyond basic intensity encryption. In this paper, we present a new method for polarization-dependent optical encryption that relies on extremely high-resolution near-field phase encoding at metasurfaces, down to the diffraction limit. Unlike previous intensity or color printing methods, which are detectable by the human eye, analog phase decoding requires specific decryption setup to achieve a higher security level. In this work, quadriwave lateral shearing interferometry is used as a phase decryption method, decrypting binary quick response (QR) phase codes and thus forming phase-contrast images, with phase values as low as 15°. Combining near-field phase imaging and far-field holographic imaging under orthogonal polarization illumination, we enhanced the security level for potential applications in the area of biometric recognition, secure ID cards, secure optical data storage, steganography, and communications.

Keywords: dielectric metasurface; information security; meta-hologram; nanoantenna; optical encryption.

1 Introduction

Information security is an important concern in daily life from civil to military applications [1, 2]. Optical encryption for information security has gained enormous attention owing to its ability to provide many degrees of freedom to encode the information relying on various optical channels such as frequency, amplitude, phase, and polarization [3, 4]. These efforts led to various encryption methods, including Lippmann plate [5], spatial correlators [6], and holograms [7]. Recently, an ultrathin artificial material with subwavelength structure called metasurface [8–10] has been developed to control the electromagnetic wave across the entire frequency range for various optical applications such as lenses [11–15], cloaking [16, 17], holograms [18–21], polarizers [22–24], perfect absorbers [25, 26], retroreflectors [27], etc. The compactness and versatile functionality make metasurfaces perfect candidates for optical encryption. The basic idea is to leverage on different optical channels of the metasurface to encode different optical information. Proof-of-concept demonstration of metasurface spectral encoding, displaying sharp and hyper-resolved images observable under a microscope, has been demonstrated [28, 29]. Metasurfaces have also been designed to perform far-field holographic encoding using the concept of meta-holograms. The latter is the most common approach in the area of metasurface encryption using different light sources to decrypt the holographic images. A great deal of attention has been paid on the design of light source–dependent meta-hologram, such as polarization selectivity [30–33], orbital angular momentum selectivity [34, 35], incoming direction of the incident light [36–38], etc. Other attempts have also been made for metasurface encryption, such as the combination of color printing and the holographic image [39, 40], image postprocessing based on spatial frequency [41], and tunable meta-hologram [42]. All of the proposed metasurface encryptions, relying either on the intensity of the color

---

***Corresponding author: Patrice Genevet**, CNRS-CRHEA, Université Cote d'Azur, Rue Bernard Gregory, Sophia Antipolis, Valbonne, 06560, France, E-mail: Patrice.Genevet@crhea.cnrs.fr
Qinghua Song, Samira Khadir, Stéphane Vézian, Benjamin Damilano, Philippe de Mierry, Sébastien Chenot and Virginie Brandli: CNRS-CRHEA, Université Cote d'Azur, Rue Bernard Gregory, Sophia Antipolis, Valbonne, 06560, France. https://orcid.org/0000-0002-4622-0418 (Q. Song)
Romain Laberdesque and Benoit Wattellier: Phasics Company, Bâtiment Explorer, Espace Technologique, Route de l'Orme des Merisiers, St. Aubin, 91190, France

print or on the holographic image projection, are directly perceived by human eyes, which could limit their applicability for information security.

Here, we introduce a new class of optical encryption that combines the near- and far-field information. On the one hand, the near-field encryption is based on phase imaging at the metasurface plane. The information is encoded in the phase of the transmitted light without any modulation of its intensity, making the information inaccessible with a conventional microscope. In order to resolve the encoded information, one has to obtain the phase map information, which we measured in this article using quadriwave lateral shearing interferometry (QLSI) technique [43–46] (see more details in Section 5). The phase-addressing capability of metasurfaces, i.e., the spatial phase distribution of the phase elements, can be scaled down to the single pixel with a pitch of 300 nm, which is beyond Abbe's classical diffraction limit with an incident wavelength higher than 600 nm. Obviously, as to retrieve the phase information, one is using traditional optical characterization tools generally limited to diffraction limits, and it is not necessary to encode with such offensive resolution. As a proof of concept, we have considered phase pixels of about 750 nm. The proposed phase encryption could complement the class of color printing at the optical diffraction limit [28, 29] in high-density spectrally encoded optical data storage and so on. On the other hand, far-field encryption relying on the holographic image requires a full 2π phase range, which according to our results, appears to be not necessary for near-field encoding mentioned above, allowing more flexibility for realistic applications. The combination of phase and projected intensity, respectively encoded in the near field and far field, improves optical information security.

In the following section, we describe the theoretical design as well as the experimental fabrication and characterization methods. Two different examples of phase encryption are demonstrated in Section 3. The first example shows several functional phase-encoded binary quick response (QR) codes with decreasing phase-encoding values ranging from 180° down to 15° phase difference, below which the experimental realization fails to deliver readable codes. In the second example, near-field encryption, i.e., phase imaging at the metasurface plane, is multiplexed with far-field encryption, i.e., holographic image projection, to display two different "Bat" and "Batman" images.

2 Design and fabrication

The principle of the dual-mode encryption is shown in Figure 1. The metasurface consists of a birefringent dielectric meta-molecule array with Jones matrix of $\begin{pmatrix} J_{xx} & 0 \\ 0 & J_{yy} \end{pmatrix} = \begin{pmatrix} e^{i\varphi_{xx}} & 0 \\ 0 & e^{i\varphi_{yy}} \end{pmatrix}$ (assuming full transmission of the incident wave). When a plane wave with x-polarization

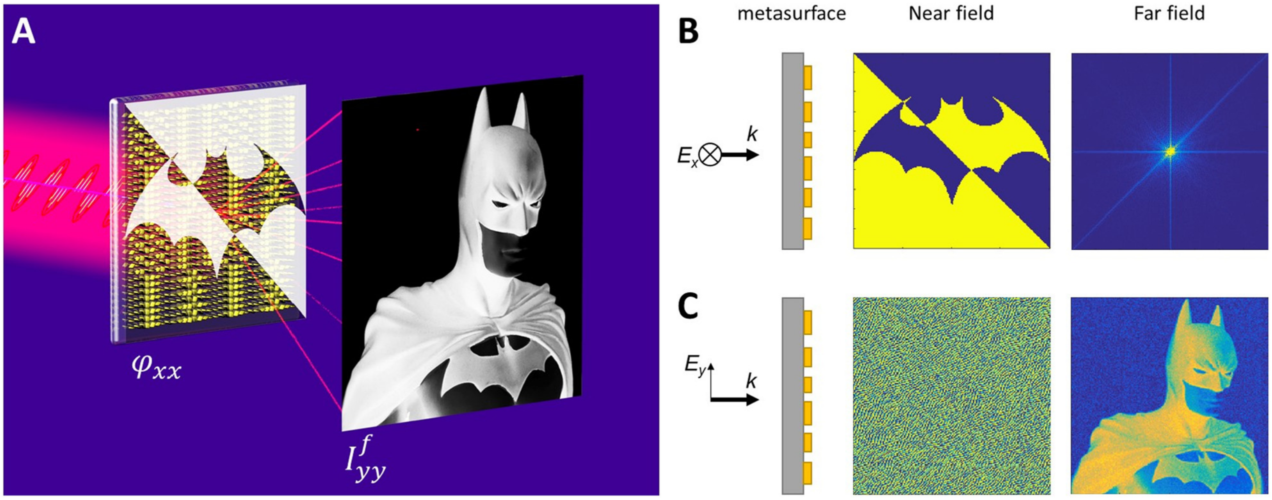

Figure 1: Design principle of dual-mode encryption combining near-field phase imaging and far-field holographic image projection. (A) Schematic of the dual-mode encryption, in which the near field is encrypted by a phase imaging of "Bat" and the far field is encrypted by a holographic image of "Batman." (B) Metasurface under x-polarized incidence (left panel). A phase imaging of "Bat" is retrieved by extracting the metasurface spatial phase distribution (middle panel). A random intensity profile is displayed in the far field (right panel). (C) Metasurface under y-polarized incidence (left panel). Complex holographic phase imaging is observed (middle panel). A holographic image of "Batman" is observed in the far field (right panel). "Bat" and "Batman" images are adapted from Wikemedia.org and Pexels.com, respectively.

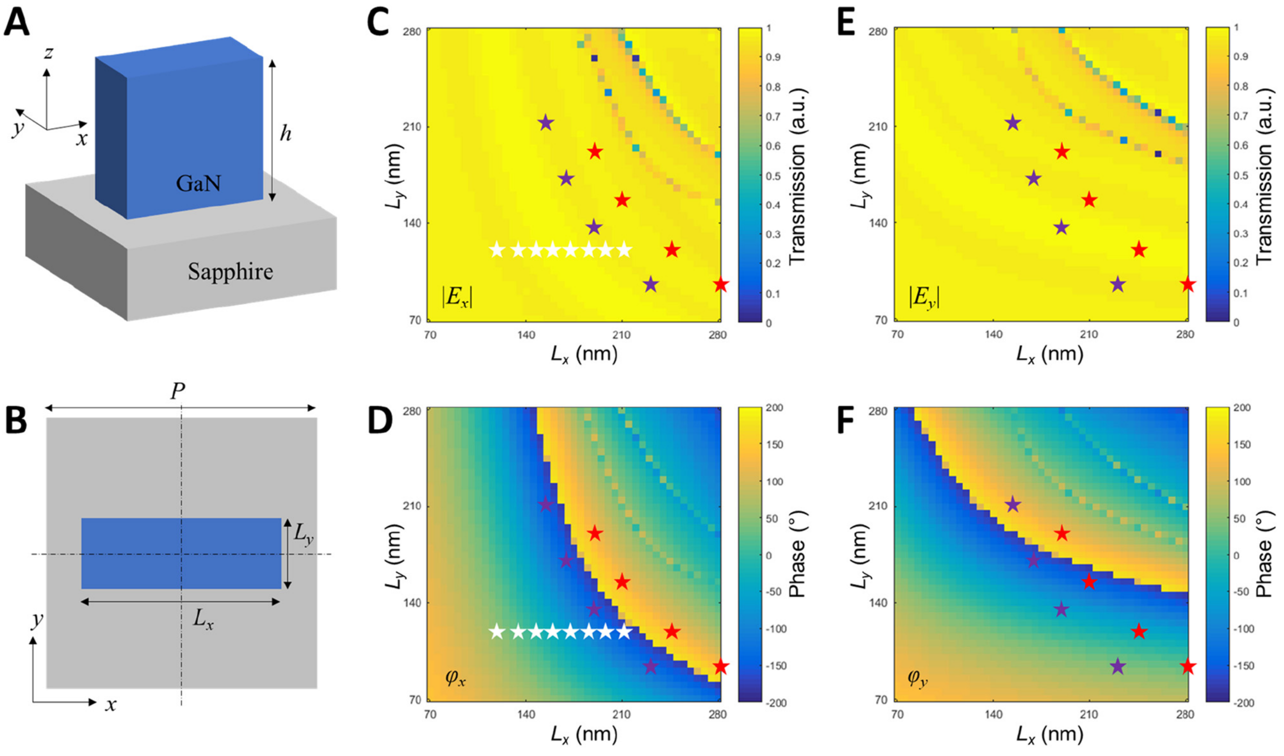

Figure 2: Simulation results of metasurface consisting of GaN nanopillars on sapphire substrate.
(A) Perspective view and (B) top view of the metasurface with one meta-molecule. (C) Simulated amplitude and (D) phase of the transmission with x-polarized incidence. (E) Simulated amplitude and (F) phase of the transmission with y-polarized incidence by changing the size of the GaN blocks. The white stars are the selected structures for the design of SC-MS. The purple and red stars are selected for the design of DC-MS. DC-MS: dual-channel metasurface; SC-MS: single-channel metasurface.

($\mathbf{E_x}$) illuminates the metasurface, as shown in Figure 1B (left panel), the output near field of the metasurface is $\mathbf{E_x}e^{i\varphi_{xx}}$, which is encoded by a phase information of φ_{xx}. By locally designing different metastructures, we can get a specific phase pattern in the near field (Figure 1B, middle) and a random intensity profile in the far field (Figure 1B, right). However, the y-polarized light works in the opposite way, creating a disordered near-field phase image but encrypting a holographic image in the far field, as shown in Figure 1C.

The design of the metasurfaces is realized using full-wave finite-difference time-domain simulations at the wavelength of 617 nm. The unit cell of the metasurface consists of semiconductor-based GaN nanopillars with a thickness of $h = 1$ µm and period of $P = 300$ nm on sapphire substrate, as shown in Figure 2A and 2B. GaN has the merits of (1) low loss in the entire visible range to design the metasurfaces with high efficiency and (2) high refractive index to manipulate the phase in the full 2π range using relatively short nanostructures. Other low loss and high refractive index like SiN and TiO_2 could be alternative choices [47, 48]. The GaN nanopillars support waveguide-like modes for which the accumulated phase of the transmitted light is strongly dependent on the dimensions L_x and L_y [13]. The simulated results of the transmitted amplitude and phase, as shown in Figure 2C–2E, demonstrate that the transmitted amplitude of the metasurface is almost near unity, while the phase is widely covering a full 2π range.

In this study, we propose two sets of encrypting metasurfaces, (1) a single-channel metasurface (SC-MS) encryption working only for x-polarized light and (2) a dual-channel metasurface (DC-MS) encryption that works differently for x- and y-polarized light. SC-MS keeps $L_y = 120$ nm, and L_x is controlled to achieve different phase information for x-polarized light, as shown by the white stars in Figure 2C and 2D. DC-MS controls both phase information of x- and y-polarized light, as shown in the purple and red stars in Figure 2C–2F. By controlling the size of L_x and L_y of the DC-MS, the transmitted phase of x-polarized light φ_{xp} and φ_{xr} (subscript "p" indicating purple stars and "r" indicating red stars) is constant along the purple and red stars, respectively, with a phase difference $\varphi_{xp} - \varphi_{xr}$ of 90° for binary phase imaging in the near field. Meanwhile, the phase of the y-polarized light φ_{yp} and φ_{yr} varies in the 2π range for the phase encoding of the holographic image in the far field. For simplicity, the holographic phase profile has been encoded in only four phase levels.

3 Results and discussion

As a proof of concept, we demonstrate a binary QR code in the SC-MS with the binary encoded phase of φ_h and φ_l (subscripts “h” and “l” indicating high- and low-level phase, respectively) for phase imaging. The QR code consists of 29 × 29 pixels with the binary phase of φ_h and φ_l, which redirects to the CNRS-CRHEA website when it is scanned using a portable QR code scanner. Each pixel of the QR code contains 20 × 20 metastructures. Thus, the total size of the SC-MS is 174 × 174 μm. We fabricate seven samples of SC-MS with different phase contrast $\Delta\varphi = \varphi_h - \varphi_l$ ranging from 5°, 15°, 30°, 60°, 90°, 135°, to 180°. The measurement setup for phase imaging is shown in Figure 3 (see more details in Section 5.2). The measured amplitude and phase profile using QLSI are shown in Figure 4A and 4B, respectively. One can see that the QR codes are almost invisible on the amplitude images and are thus impossible to read while they are clearly visible on the phase images. When the phase contrast $\Delta\varphi \geq 15°$, the measured QR code phase images can be scanned and directed to the CNRS-CRHEA website, but it starts to fail when $\Delta\varphi \leq 5°$. In order to estimate the actual values of $\Delta\varphi$ of the measured QR code phase images, we plot the pixel-by-pixel

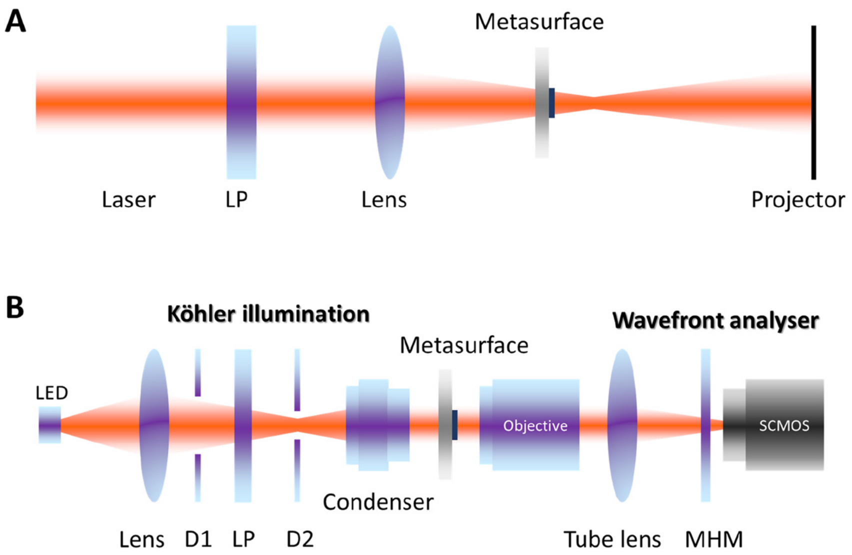

Figure 3: Measurement setup for dual-mode encryption.
(A) Optical setup for far-field holographic imaging under illumination of laser at a wavelength of 617 nm. (B) Phase imaging measurement setup using QLSI. An LED with a wavelength centered at 617 nm integrated in a Köhler configuration is used as an illumination source on the metasurface with a controlled optical plane wave. The transmitted signal is then collected by the wavefront analyzer. D1 and D2 are field and aperture diaphragms, respectively. LED: light-emitting diode; LP: linear polarizer; MHM: modified Hartmann mask; QLSI: quadriwave lateral shearing interferometry; SCMOS: scientific complementary metal-oxide-semiconductor.

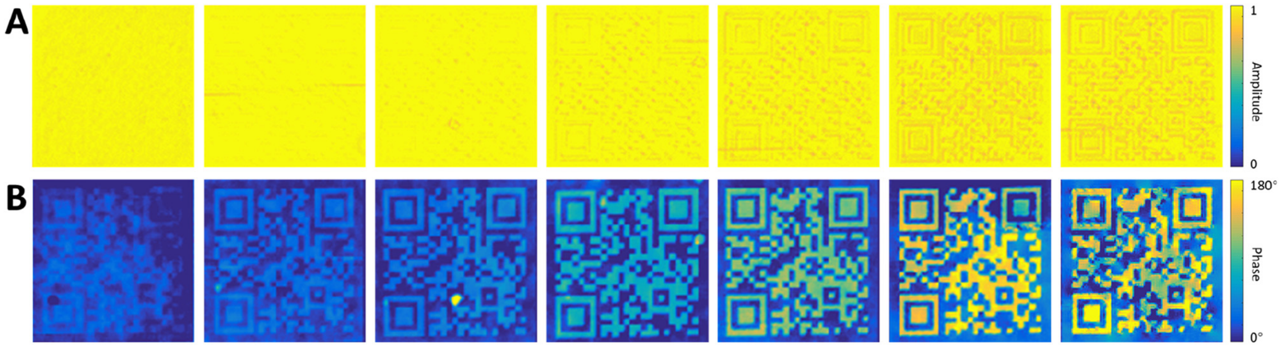

Figure 4: Experimental results of binary QR codes using SC-MS.
(A) Amplitude and (B) phase images measured by QLSI. From left to right panels, the expected binary phase contrast values are 5°, 15°, 30°, 60°, 90°, 135°, and 180° (all the phase images have the same scale of 0–180°). The QR code is designed to link the CNRS-CRHEA website (www.crhea.cnrs.fr). The phase images with binary phase contrast ≥15° can be redirected to the CNRS-CRHEA website when scanned by a portable QR code scanner, and it starts to fail for extremely small phase contrast below 5°. The size of the QR code is 174 × 174 μm. QLSI: quadriwave lateral shearing interferometry; QR: quick response; SC-MS: single-channel metasurface.

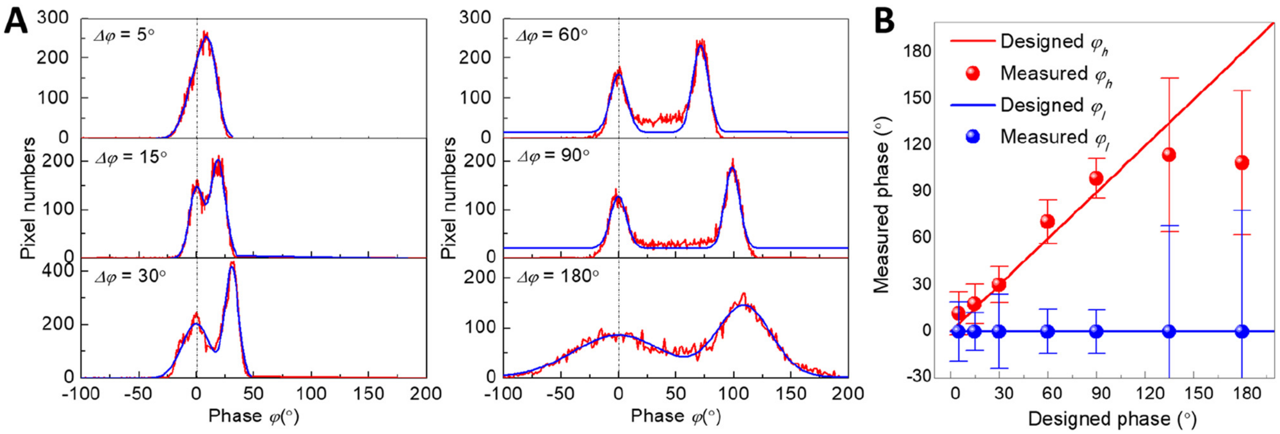

Figure 5: (A) Pixel-by-pixel histogram of the measured phase images for the different designed phase contrast of 5°, 15°, 30°, 60°, 90°, and 180°. Red curve: measured results. Blue curve: fitting curves based on two Gaussian functions. (B) The measured phase and standard deviation of binary phase imaging.

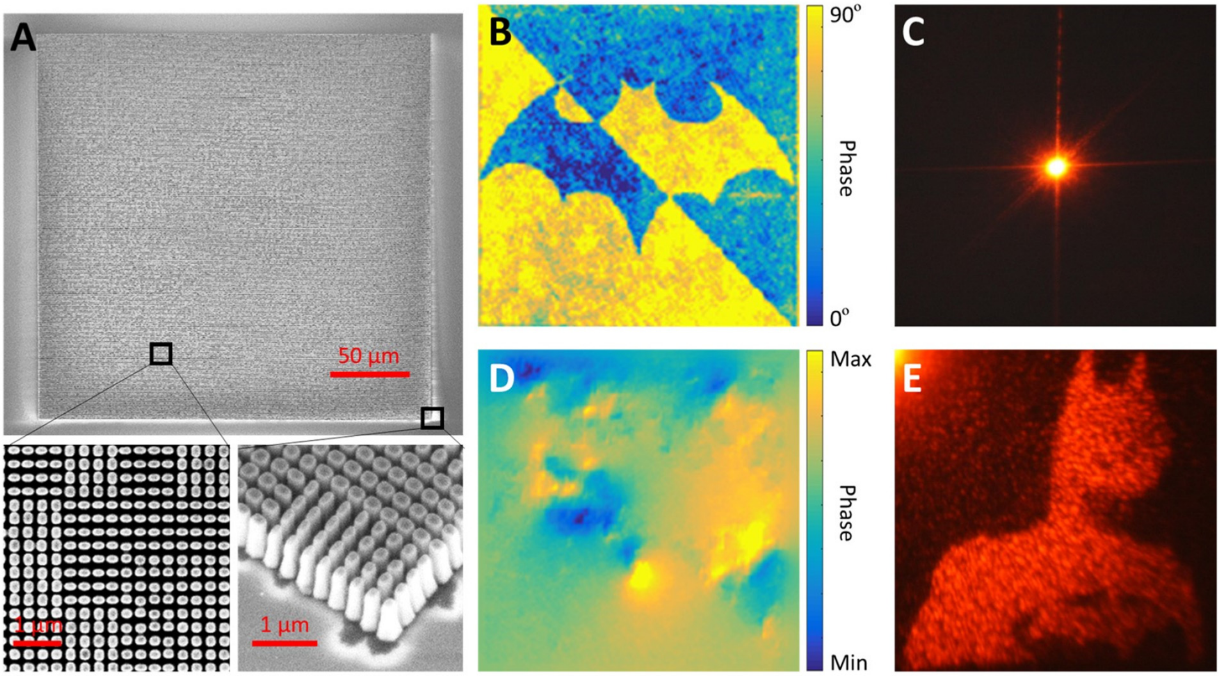

Figure 6: Experimental results of DC-MS.
(A) SEM images of the fabricated metasurface. (B) Measured phase image and (C) far-field image with *x*-polarized incidence. (D) Measured phase image and (E) far-field holographic image with *y*-polarized incidence. DC-MS: dual-channel metasurface; SEM: scanning electron microscopy.

histograms for each image, as shown in Figure 5A. The histogram is fitted with Gaussian functions with two peaks, one corresponding to the low-level phase φ_l and the other corresponding to the high-level phase φ_h. The difference between the two peaks gives the phase contrast $\Delta\varphi$, while the full width at half maximum estimates the error of the extracted phase. The results for different phase contrast from 15° to 180° are shown in Figure 5A. The expected measured phase and standard deviation of φ_h and φ_l are shown in Figure 5B.

It can be seen that when $\Delta\varphi$ is too small, $\Delta\varphi = 5°$, the width of each Gaussian profile is larger than $\Delta\varphi$, which makes the two peaks indistinguishable. The discrepancy of the measured phase mainly comes from the fabrication error because the length difference of the GaN nanopillars corresponding to the binary phase of 5° is only 2.5 nm, which is lower than our electron-beam lithography (EBL) precision. Increasing the designed phase contrast, i.e., such as $\Delta\varphi \geq 15°$, the two peaks become distinguishable, and the extracted phase contrasts agree well with the expected ones. However, when the phase contrast is close to 180°, such as $\Delta\varphi = 135°$ and $\Delta\varphi = 180°$, the standard deviation is increasing owing to the phase wrapping issues from the phase retrieval algorithm used to extract the pixel phase value.

The near-field phase imaging can be further combined with far-field holographic imaging so that a dual-mode optical encryption can be achieved. Here, the phase contrast of near-field phase imaging is chosen as $\Delta\varphi = 90°$, according to its good performance shown in Figure 5. The experimental results of DC-MS for near-field and far-field encryption are shown in Figure 6A. When the metasurface is illuminated by *x*-polarized light, a phase image of "Bat" measured by QLSI is shown in Figure 6B; however, owing to the designed phase in the near field only, the holographic image in the far field has no useful information, as shown in Figure 6C. Instead, considering a *y*-polarized light illumination, a phase profile without useful information is shown in Figure 6D, displaying a holographic image of "Batman" in the far field, as shown in Figure 6E, to achieve a dual-mode optical encryption able to combine near-field phase imaging and far-field holographic image projection.

4 Conclusion

In conclusion, we have demonstrated a new class of optical encryption relying on dual-mode metasurfaces. Our method is able to print optical phase information at the nanoscale, which can be extracted using QLSI technique. We encoded several phase QR codes in simple binary phase images, demonstrating significant advantage with respect to conventional full-phase holographic image encryption. We demonstrated that a phase difference as low as 15° is sufficient to successfully scan the QR code and redirect to the desired website page. It is interesting to point out that gradually varying the nanopillar geometry enables analog phase addressing, offering an interesting perspective for multiplexed coding capabilities. Moreover, by combining the holographic display in the orthogonal polarization, a dual-mode optical encryption is demonstrated for near-field and far-field encryption, expanding promising applications in optical information security, data encryption, optical ID tags for authentication and verification, high-density optical data storage, etc.

5 Methods

5.1 Fabrication processes

The fabrication of the metasurface starts from growing a 1-μm GaN thin film on a double-side polished *c*-plane sapphire substrate using a molecular beam epitaxy RIBER system. Conventional EBL is used to pattern the GaN nanopillars. The GaN thin film is spin-coated by a double layer of 200-nm Polymethyl methacrylate (PMMA) resist (495A4) and baked on a hot plate at a temperature of 125 °C. The resist is exposed to an electron beam of 20 keV (Raith ElphyPlus, Zeiss Supra 40) considering the desired pattern and then developed using IPA:MIBK (3:1) solution. A 50-nm-thick nickel film is deposited on the sample in the e-beam evaporator, and a nickel hard mask is obtained by removing the resist through the lift-off process in acetone solution. The GaN nanopillars are obtained by reactive ion etching (Oxford system) with a plasma composed of Cl_2CH_4Ar gases. Finally, the nickel hard mask on the GaN nanopillars is dissolved in $HCl{:}HNO_3$ (1:2) solution, revealing only the GaN nanopillar pattern on the transparent sapphire substrate.

5.2 Measurement setup

The measurement setup for far-field holographic imaging is shown in Figure 3A. A laser with a wavelength of 617 nm is used as the light source. The latter passes through a linear polarizer followed by a lens to weakly focus on the metasurface and creates a holographic image in the far field, which is captured by a projector placed after the metasurface at a distance of 10 cm. The setup for phase imaging is shown in Figure 3B. It utilizes a quantitative phase microscopy technique based on QLSI [42–45]. A light-emitting diode with a wavelength centered at 617 nm integrated in a Köhler configuration is used as an illumination source with a controlled optical plane wave (controlled illuminated area and controlled numerical aperture). The light beam passing through the metasurface is collected by a microscope objective and sent to the QLSI wavefront analyzer (SID4 camera from Phasics Company) to measure both the intensity and the optical path difference of the light at the microscope's imaging plane, coinciding with the metasurface position.

Acknowledgments: The authors acknowledge the support from the European Research Council (ERC) under the European Union's Horizon 2020 research and innovation program (grant agreement no. 639109).

Author contribution: All the authors have accepted responsibility for the entire content of this submitted manuscript and approved submission.

Research funding: The study was supported from the European Research Council (ERC) under the European Union's Horizon 2020 research and innovation program (grant agreement no. 639109).

Conflict of interest statement: The authors declare no conflicts of interest regarding this article.

References

[1] R. Anderson and T. Moore, “The economics of information security,” *Science*, vol. 314, pp. 610–613, 2006.

[2] M. E. Whitman and H. J. Mattord, *Principles of Information Security*, Boston, Cengage Learning, 2011. ISBN10: 1-337-10206-7; ISBN13: 978-1-337-10206-3.

[3] O. Matoba, T. Nomura, E. Perez-Cabre, M. S. Millan, and B. Javidi, “Optical techniques for information security,” *Proc. IEEE*, vol. 97, pp. 1128–1148, 2009.

[4] B. Javidi, Ed. *Optical and Digital Techniques for Information Security*, New York, Springer, 2005.

[5] G. Lippmann, “Sur la théorie de la photographie des couleurs simples et composées par la méthode interférentielle,” *J. Phys. Theor. Appl.*, vol. 3, pp. 97–107, 1894.

[6] Y. Li, K. Kreske, and J. Rosen, “Security and encryption optical systems based on a correlator with significant output images,” *Appl. Opt, AO*, vol. 39, pp. 5295–5301, 2000.

[7] O. Bryngdahl and F. Wyrowski, “I digital holography – computer-generated holograms. In: Wolf E., Ed., editor. Progress in Optics, 28. Amsterdam, Netherlands: Elsevier; 1990. pp. 1–86.

[8] N. Yu, P. Genevet, M. A. Kats, et al., “Light propagation with phase discontinuities: generalized laws of reflection and refraction,” *Science*, vol. 334, pp. 333–337, 2011.

[9] N. Yu and F. Capasso, “Flat optics with designer metasurfaces,” *Nat. Mater.*, vol. 13, pp. 139–150, 2014.

[10] P. Genevet, F. Capasso, F. Aieta, M. Khorasaninejad, and R. Devlin, “Recent advances in planar optics: from plasmonic to dielectric metasurfaces,” *Optica*, vol. 4, 2017, pp. 139–152.

[11] M. Khorasaninejad and F. Capasso, “Metalenses: Versatile multifunctional photonic components,” *Science*, vol. 358, p. eaam8100, 2017.

[12] W. T. Chen, A. Y. Zhu, V. Sanjeev, et al., “A broadband achromatic metalens for focusing and imaging in the visible,” *Nat. Nanotechnol.*, vol. 13, pp. 220–226, 2018.

[13] S. Wang, P. C. Wu, V.-C. Su, et al., “A broadband achromatic metalens in the visible,” *Nat. Nanotechnol.*, vol. 13, pp. 227–232, 2018.

[14] C. Sun, “Shrinking the camera size: metasurface lens,” *Nat. Mater.*, vol. 16, pp. 11–12, 2017.

[15] W. M. Zhu, Q. Song, L. Yan, et al., “A flat lens with tunable phase gradient by using random access reconfigurable metamaterial,” *Adv. Mater.*, vol. 27, pp. 4739–4743, 2015.

[16] J. Y. H. Teo, L. J. Wong, C. Molardi, and P. Genevet, “Controlling electromagnetic fields at boundaries of arbitrary geometries,” *Phys. Rev. A*, vol. 94, 2016, Art no. 023820.

[17] Y. Y. Xie, P. N. Ni, Q. H. Wang, et al., “Metasurface-integrated vertical cavity surface-emitting lasers for programmable directional lasing emissions,” *Nat. Nanotechnol.*, vol. 15, pp. 125–130, 2020.

[18] G. Zheng, H. Mühlenbernd, M. Kenney, G. Li, T. Zentgraf, and S. Zhang, “Metasurface holograms reaching 80% efficiency,” *Nat. Nanotechnol.*, vol. 10, pp. 308–312, 2015.

[19] P. Genevet, J. Lin, M. A. Kats, and F. Capasso, “Holographic detection of the orbital angular momentum of light with plasmonic photodiodes,” *Nat. Commun.*, vol. 3, p. 1278, 2012.

[20] L. Huang, X. Chen, H. Mühlenbernd, et al., “Three-dimensional optical holography using a plasmonic metasurface,” *Nat. Commun.*, vol. 4, p. 2808, 2013.

[21] Q. Song, A. Baroni, R. Sawavt, et al., “Ptychography retrieval of fully polarized holograms from geometric-phase metasurfaces,” *Nat. Commun.*, vol. 11, pp. 1–8, 2020.

[22] J. K. Gansel, M. Thiel, M. S. Rill, et al., “Gold helix photonic metamaterial as broadband circular polarizer,” *Science*, vol. 325, pp. 1513–1515, 2009.

[23] Q. H. Song, P. C. Wu, W. M. Zhu, et al., “Split Archimedean spiral metasurface for controllable GHz asymmetric transmission,” *Appl. Phys. Lett.*, vol. 114, p. 151105, 2019.

[24] Y. Z. Shi, T. Zhu, T. Zhang, et al., “Chirality-assisted lateral momentum transfer for bidirectional enantioselective separation,” *Light Sci. Appl.*, vol. 9, pp. 1–12, 2020.

[25] G. M. Akselrod, J. Huang, T. B. Hoang, et al., “Large-area metasurface perfect absorbers from visible to near-infrared,” *Adv. Mater.*, vol. 27, pp. 8028–8034, 2015.

[26] Q. Song, W. M. Zhu, P. C. Wu, et al., “Liquid-metal-based metasurface for terahertz absorption material: frequency-agile and wide-angle,” *APL Mater.*, vol. 5, p. 066103, 2017.

[27] L. Yan, W. M. Zhu, M. F. Karim, et al., “0.2 λ_0 thick adaptive retroreflector made of spin-locked metasurface,” *Adv. Mater.*, vol. 30, p. 1802721, 2018.

[28] K. Kumar, H. Duan, R. S. Hegde, S. C. Koh, J. N. Wei, and J. K. Yang, “Printing colour at the optical diffraction limit,” *Nat. Nanotechnol.*, vol. 7, pp. 557–561, 2012.

[29] Y. Gu, L. Zhang, J. K. Yang, S. P. Yeo, and C. W. Qiu, “Color generation via subwavelength plasmonic nanostructures,” *Nanoscale*, vol. 7, pp. 6409–6419, 2015.

[30] X. Luo, Y. Hu, X. Li, et al., “Integrated metasurfaces with microprints and helicity-multiplexed holograms for real-time optical encryption,” *Adv. Opt. Mater.*, vol. 8, p. 1902020, 2020.

[31] R. Zhao, L. Huang, C. Tang, et al., “Nanoscale polarization manipulation and encryption based on dielectric metasurfaces,” *Adv. Opt. Mater.*, vol. 6, p. 1800490, 2018.

[32] J. Deng, L. Deng, Z. Guan, et al., “Multiplexed anticounterfeiting meta-image displays with single-sized nanostructures,” *Nano Lett.*, vol. 20, pp. 1830–1838, 2020.

[33] L. Deng, J. Deng, Z. Guan, et al., “Malus-metasurface-assisted polarization multiplexing,” *Light Sci. Appl.*, vol. 9, p. 101, 2020.

[34] H. Ren, G. Briere, X. Fang, et al., “Metasurface orbital angular momentum holography,” *Nat. Commun.*, vol. 10, p. 2986, 2019.

[35] X. Fang, H. Ren, and M. Gu, “Orbital angular momentum holography for high-security encryption,” *Nat. Photon.*, vol. 14, pp. 102–108, 2020.

[36] K. Chen, G. Ding, G. Hu, et al., “Directional Janus metasurface,” *Adv. Mater.*, vol. 32, p. 1906352, 2020.

[37] Y. Chen, X. Yang, and J. Gao, “3D Janus plasmonic helical nanoapertures for polarization-encrypted data storage,” *Light Sci. Appl.*, vol. 8, p. 45, 2019.

[38] D. Frese, Q. Wei, Y. Wang, L. Huang, and T. Zentgraf, “Nonreciprocal asymmetric polarization encryption by layered plasmonic metasurfaces,” *Nano Lett.*, vol. 19, pp. 3976–3980, 2019.

[39] G. Yoon, D. Lee, K. T. Nam, and J. Rho, ““Crypto-display” in dual-mode metasurfaces by simultaneous control of phase and spectral responses,” *ACS Nano*, vol. 12, pp. 6421–6428, 2018.

[40] K. T. P. Lim, H. Liu, Y. Liu, and J. K. W. Yang, “Holographic colour prints for enhanced optical security by combined phase and amplitude control,” *Nat. Commun.*, vol. 10, p. 25, 2019.

[41] J. Deng, Y. Yang, J. Tao, et al., “Spatial frequency multiplexed meta-holography and meta-nanoprinting,” *ACS Nano*, vol. 13, pp. 9237–9246, 2019.

[42] J. Li, S. Kamin, G. Zheng, F. Neubrech, S. Zhang, and N. Liu, "Addressable metasurfaces for dynamic holography and optical information encryption," *Sci. Adv.*, vol. 4, p. eaar6768, 2018.

[43] P. Bon, G. Maucort, B. Wattellier, and S. Monneret, "Quadriwave lateral shearing interferometry for quantitative phase microscopy of living cells," *Opt. Express*, vol. 17, p. 13080, 2009.

[44] S. Khadir, D. Andrén, P. C. Chaumet, et al., "Full optical characterization of single nanoparticles using quantitative phase imaging," *Optica*, vol. 7, p. 243, 2020.

[45] S. Khadir, D. Andrén, D. Verre, et al., "optical imaging and characterization of graphene and other 2D materials using quantitative phase microscopy," *ACS Photonics*, vol. 4, no. 12, pp. 3130–3139, 2017.

[46] J. Primot and N. Guérineau, "Extended Hartmann test based on the pseudoguiding property of a Hartmann mask completed by a phase chessboard," *Appl. Optic.*, vol. 39, pp. 5715–5720, 2000.

[47] S. Colburn, A. Zhan, E. Bayati, et al., "Broadband transparent and CMOS-compatible flat optics with silicon nitride metasurfaces," *Opt. Mater. Express*, vol. 8, pp. 2330–2343, 2018.

[48] M. Khorasaninejad, W. T. Chen, R. C. Devlin, J. Oh, A. Y. Zhu, and F. Capasso, "Metalenses at visible wavelengths: diffraction-limited focusing and subwavelength resolution imaging," *Science*, vol. 352, pp. 1190–1194, 2016.